

Orbital selective spin excitations and their impact on superconductivity of $\text{LiFe}_{1-x}\text{Co}_x\text{As}$

Yu Li,¹ Zhiping Yin,^{2,3,*} Xiancheng Wang,⁴ David W. Tam,¹ D. L. Abernathy,⁵
A. Podlesnyak,⁵ Chenglin Zhang,¹ Meng Wang,⁶ Lingyi Xing,⁴ Changqing Jin,^{4,7}
Kristjan Haule,³ Gabriel Kotliar,³ Thomas A. Maier,⁸ and Pengcheng Dai^{1,2,†}

¹*Department of Physics and Astronomy, Rice University, Houston, Texas 77005, USA*

²*Center for Advanced Quantum Studies and Department of Physics,
Beijing Normal University, Beijing 100875, China*

³*Department of Physics, Rutgers University, Piscataway, New Jersey 08854, USA*

⁴*Beijing National Laboratory for Condensed Matter Physics,
Institute of Physics, Chinese Academy of Sciences, Beijing 100190, China*

⁵*Quantum Condensed Matter Division, Oak Ridge National Laboratory, Oak Ridge, Tennessee 37831, USA*

⁶*Department of Physics, University of California, Berkeley, California 94720, USA*

⁷*Collaborative Innovation Center of Quantum Matter, Beijing, China*

⁸*Center for Nanophase Materials Sciences and Computer Science and Mathematics Division,
Oak Ridge National Laboratory, Oak Ridge, Tennessee 37831, USA*

(Dated: August 31, 2018)

We use neutron scattering to study spin excitations in single crystals of $\text{LiFe}_{0.88}\text{Co}_{0.12}\text{As}$, which is located near the boundary of the superconducting phase of $\text{LiFe}_{1-x}\text{Co}_x\text{As}$ and exhibits non-Fermi-liquid behavior indicative of a quantum critical point. By comparing spin excitations of $\text{LiFe}_{0.88}\text{Co}_{0.12}\text{As}$ with a combined density functional theory (DFT) and dynamical mean field theory (DMFT) calculation, we conclude that wave-vector correlated low energy spin excitations are mostly from the d_{xy} orbitals, while high-energy spin excitations arise from the d_{yz} and d_{xz} orbitals. Unlike most iron pnictides, the strong orbital selective spin excitations in LiFeAs family cannot be described by anisotropic Heisenberg Hamiltonian. While the evolution of low-energy spin excitations of $\text{LiFe}_{1-x}\text{Co}_x\text{As}$ are consistent with electron-hole Fermi surface nesting condition for the d_{xy} orbital, the reduced superconductivity in $\text{LiFe}_{0.88}\text{Co}_{0.12}\text{As}$ suggests that Fermi surface nesting conditions for the d_{yz} and d_{xz} orbitals are also important for superconductivity in iron pnictides.

PACS numbers: 74.70.Xa, 75.30.Gw, 78.70.Nx

Superconductivity in iron pnictides occurs near the vicinity of an antiferromagnetic (AF) instability [1–5]. One exception is LiFeAs , which exhibits superconductivity at $T_c = 18$ K without an AF ordered parent compound [6–8]. Although magnetism is generally believed to play a central role in the superconductivity of iron pnictides [4, 5], the unique nature of LiFeAs has raised considerable debates concerning whether magnetism is indeed fundamental to the superconductivity of iron-based superconductors. There are two important issues to be addressed. The first is whether magnetism and superconductivity in LiFeAs can arise from quasiparticle excitations between hole and electron nested Fermi surfaces similar to other iron pnictide superconductors [9–11]. The second concerns the impact of orbital degrees of freedom on the superconductivity of LiFeAs [12, 13].

In most iron pnictides, Fe ions are in a d^6 configuration with five same-spin electrons in the e_g and t_{2g} orbitals, and one remaining opposite-spin electron fluctuating among all the d orbitals, due to the large Hund's rule coupling, although there is a considerable (but smaller) crystal-field splitting between the e_g and t_{2g} orbitals [14–20]. The t_{2g} electrons near the Fermi level occupy the d_{xy} and degenerate d_{xz}/d_{yz} orbitals. In the undoped state, low-energy spin excitations in LiFeAs are trans-

versely incommensurate from the AF ordering wave vector of iron pnictides such as BaFe_2As_2 [Fig 1(a) and Fig. 1(b)] [3], consistent with nested Fermi surfaces from either the large d_{xy} or small d_{yz}/d_{xz} hole pocket near Γ point in reciprocal space to electron pockets near M points [Fig. 1(c) and Fig. 1(e)] [21–23]. When Co is doped into LiFeAs to form $\text{LiFe}_{1-x}\text{Co}_x\text{As}$, superconductivity is gradually suppressed with increasing Co doping and vanishes near $x = 0.14$ [24], and the system becomes paramagnetic for higher Co-doping levels [Fig. 1(a)] [25]. From angle resolved photoemission spectroscopy (ARPES) [26, 27], it was found that Co-doping introduces electrons to LiFeAs , reduces the size of the d_{xy} hole Fermi surface, moves the small d_{yz}/d_{xz} hole pockets below the Fermi surface, and enlarges the electron pockets [Fig. 1(d)]. While the hole-electron Fermi surface nesting condition is improved for the d_{xy} orbitals near $x = 0.12$, Fermi surface nesting is no longer possible for the d_{yz}/d_{xz} orbitals [Fig. 1(d)]. Since transport, optical spectroscopy, and nuclear magnetic resonance measurements on $\text{LiFe}_{1-x}\text{Co}_x\text{As}$ find enhanced low-energy spin fluctuations near $x = 0.12$ with non-Fermi liquid behavior, these results were taken as evidence that spin fluctuations due to enhanced Fermi surface nesting can give rise to the observed non-Fermi liquid behavior, but are

not important for superconductivity of LiFeAs [25].

In this Letter, we present inelastic neutron scattering study and a combined density functional theory (DFT) and dynamical mean field theory (DMFT) calculation of spin excitations in LiFe_{0.88}Co_{0.12}As. While low-energy spin excitations in LiFe_{0.88}Co_{0.12}As indeed become commensurate consistent with improved electron-hole Fermi surface nesting condition for the d_{xy} orbitals [Fig. 1(d)], the absence of the hole Fermi pockets near the Γ point prevents the electron-hole nesting between the d_{yz}/d_{xz} orbitals. Since our DFT+DMFT calculations suggest a strongly correlated d_{xy} orbital with much reduced magnetic bandwidth and effective exchange coupling (Fig. 2, 3, 4), the improved nesting condition in LiFe_{0.88}Co_{0.12}As, while sufficient to induce the observed non-Fermi liquid behavior [25] and increased magnetic excitations near the AF wave vector, is insufficient to cause superconductivity due to increased incoherent electronic state of the d_{xy} band in Co-doped LiFeAs [26]. Similarly, we find that spin excitations at higher energies with much steeper dispersion arise mostly from electron-hole quasi-particle excitations of the d_{yz}/d_{xz} orbitals with much larger magnetic bandwidth and effective exchange coupling compared with NaFeAs (Fig. 4) [28]. Therefore, spin excitations in the LiFeAs family are highly orbital selective. While spin waves in many iron pnictides can be well described by an anisotropic Heisenberg Hamiltonian [5], the spin excitations in the LiFeAs family cannot be satisfactorily explained by such a model. Our results thus suggest that the occurrence of superconductivity in LiFe_{1-x}Co_xAs requires Fermi surface nesting of the d_{xz}/d_{yz} orbitals.

Our inelastic neutron scattering measurements on LiFeAs and LiFe_{0.88}Co_{0.12}As were carried out at the wide Angular-Range Chopper Spectrometer (ARCS) and Cold Neutron Chopper Spectrometer (CNCS) at Spallation Neutron Source, Oak Ridge National Laboratory. Single crystals of LiFeAs (3.95-g) and LiFe_{0.88}Co_{0.12}As (7.58-g) are grown using flux method with ⁷Li isotope. We define the momentum transfer \mathbf{Q} in three-dimensional reciprocal space in \AA^{-1} as $\mathbf{Q} = H\mathbf{a}^* + K\mathbf{b}^* + L\mathbf{c}^*$, where H , K , and L are Miller indices and $\mathbf{a}^* = \hat{\mathbf{a}}2\pi/a$, $\mathbf{b}^* = \hat{\mathbf{b}}2\pi/b$, $\mathbf{c}^* = \hat{\mathbf{c}}2\pi/c$ with $a = b \approx 5.316 \text{ \AA}$, and $c = 6.306 \text{ \AA}$ for both samples. In this notation, the AF Bragg peaks for magnetically ordered compound NaFeAs should occur at $\mathbf{Q}_{AF} = (\pm 1, 0, L)$ ($L = 0.5, 1.5, \dots$) positions in reciprocal space [Fig. 1(e) and 1(f)] [30]. Samples are co-aligned in the $[H, 0, L]$ scattering plane with mosaic less than 3° and incident beam ($E_i = 20, 35, 80, 250, 450 \text{ meV}$) parallel to the c -axis of the crystals [31].

We first compare low energy spin excitations in pure LiFeAs ($T_c \approx 18 \text{ K}$) and LiFe_{0.88}Co_{0.12}As ($T_c \approx 4 \text{ K}$). Figure 2(a) shows image of the $E = 7 \pm 1 \text{ meV}$ excitations near \mathbf{Q}_{AF} for LiFeAs obtained on ARCS. Consistent with earlier work [21–23], the data reveals clear transverse incommensurate spin excitations away from

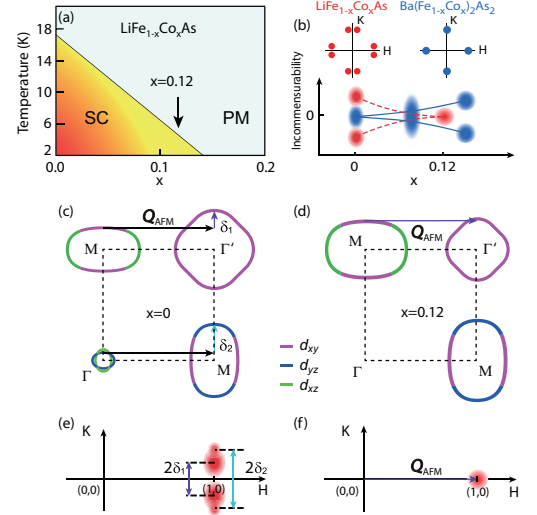


FIG. 1: (Color online) (a) Electronic phase diagram of LiFe_{1-x}Co_xAs. The superconductivity (SC) is suppressed by Co-doping and the system is in paramagnetic (PM) phase above T_c . The arrow indicates the doping level of $x = 0.12$ in our experiment [26, 27]. (b) Evolution of the low energy spin excitations in reciprocal space with electron doping for LiFeAs and BaFe_{2-x}Ni_xAs₂. Red spots indicate positions of low energy spin fluctuations in LiFe_{1-x}Co_xAs and Blue ones are for BaFe_{2-x}Ni_xAs₂ [32]. Schematics of the Fermi surfaces for LiFeAs (c) and LiFe_{0.88}Co_{0.12}As (d) [26]. Based on ARPES measurements, the mismatched hole and electron Fermi surfaces should result in the incommensurate spin excitations at δ_1 and δ_2 . (e) Positions of transverse incommensurate spin excitations of LiFeAs at $E = 10 \text{ meV}$ seen in the neutron scattering measurements [23]. (f) Commensurate spin excitations of LiFe_{0.88}Co_{0.12}As at $E = 10 \text{ meV}$.

\mathbf{Q}_{AF} as shown in the $[1, K]$ cut of Fig. 2(b). The incommensurate peaks may arise from nesting of the outer hole or inner hole Fermi surface to the electron Fermi surfaces, which give slightly different incommensurability δ_1 and δ_2 , respectively, as seen in the experiment [Fig. 1(c) and 1(e)] [22, 23]. Figure 2(c) shows identical image of constant energy ($E = 7 \pm 1 \text{ meV}$) excitations for LiFe_{0.88}Co_{0.12}As. A constant energy cut along the $[1, K]$ direction reveals that spin excitations are well defined at the commensurate wave vector \mathbf{Q}_{AF} [Fig. 2(d)]. Figure 2(e) shows the dispersion of commensurate spin excitations obtained on CNCS. The rod like feature at \mathbf{Q}_{AF} below 10 meV confirms the commensurate nature of spin excitations in LiFe_{0.88}Co_{0.12}As. To determine if weak superconductivity at $T_c = 4 \text{ K}$ has an impact on low-energy spin excitations, we show in Fig. 2(f) temperature difference plot between 2 K and 10 K . The absence of the temperature difference scattering in Fig. 2(f) below and above T_c suggests that the weak superconductivity has negligible effect on the low-energy spin excitations. Based on data in Fig. 2, we summarize in Fig. 1(b) the Co-doping evolution of the low-energy spin excitations in LiFe_{1-x}Co_xAs. Different from BaFe_{2-x}Ni_xAs₂,

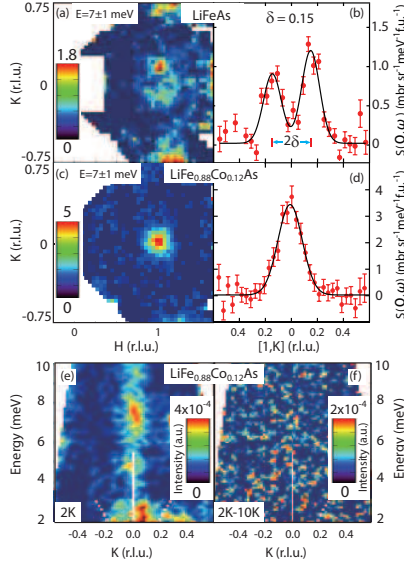


FIG. 2: (Color online) (a,c) Two-dimensional constant-energy images of spin excitations in the $[H, K]$ plane at $E = 7 \pm 1$ meV and 5 K for LiFeAs and LiFe_{0.88}Co_{0.12}As, respectively. The high scattering intensity near $(1, \pm 0.75)$ in (a) is due to phonons, but becomes less obvious in (c) due to different intensity scale. (b,d) Constant-energy cuts of spin excitations along the $[1, K]$ direction for LiFeAs and LiFe_{0.88}Co_{0.12}As at $E = 7 \pm 1$ meV, respectively. The solid lines are fits to two Gaussians for LiFeAs and a single Gaussian for LiFe_{0.88}Co_{0.12}As [31]. The intensity is in absolute units by normalizing a vanadium standard. (e) Energy-momentum plots of spin excitations along the $[1, K]$ direction integrated from $H = 0.9$ to 1.1 for LiFe_{0.88}Co_{0.12}As. The commensurate spin excitations form a vertical rod of scattering centered at $\mathbf{Q}_{AF} = (1, 0)$ point. (f) The temperature difference scattering between 2 K and 10 K.

where the low-energy spin excitations becomes transversely incommensurate with increasing Ni-doping [32], Co-doping in LiFeAs changes transversely incommensurate spin excitations to commensurate as shown in Fig. 1(b), Fig. 1(e) and 1(f). The differences in the electron doping evolution of the low-energy spin excitations between LiFe_{1-x}Co_xAs and BaFe_{2-x}Ni_xAs₂ can be understood within the Fermi surface nesting picture as due to the differences in Fermi surfaces of LiFeAs [26, 27] and BaFe₂As₂ [33]. A unique feature of the Fermi surfaces in LiFeAs is the large d_{xy} orbital hole pocket at $(1, 1)$ [Fig. 1(c)] [34]. Upon Co-doping to introduce additional electrons to LiFeAs, the large d_{xy} hole pocket shrinks and results in a better nesting with the electron pocket at $(0, 1)$, while the small d_{yz}/d_{xz} hole pocket sinks below the Fermi level [Fig. 1(c) and 1(d)]. For LiFe_{0.88}Co_{0.12}As, the observed commensurate spin excitations are consistent with this picture, and suggest that low-energy spin excitations are mostly driven from the d_{xy} orbitals. This is consistent with the random phase approximation (RPA) calculations using ARPES deter-

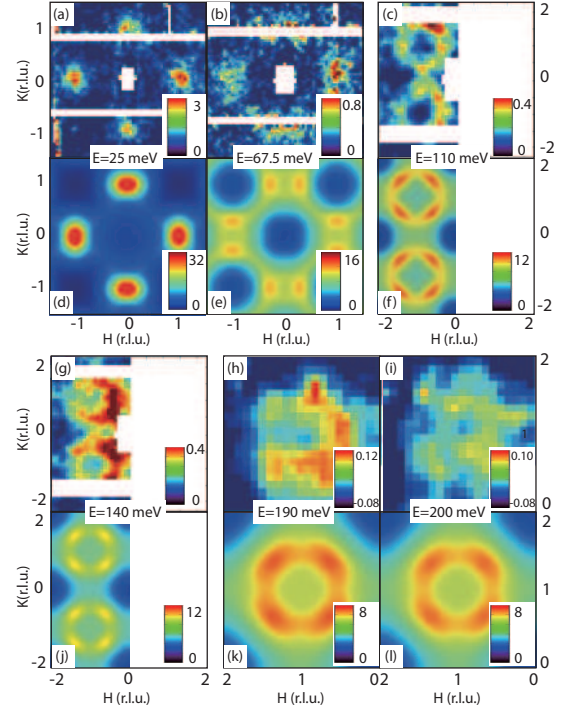


FIG. 3: (Color online) (a-c),(g-i) Constant-energy scattering images in the $[H, K]$ zones for LiFe_{0.88}Co_{0.12}As at energy transfers of $E = 25 \pm 5$ meV ($E_i = 80$ meV), 67.5 ± 7.5 meV ($E_i = 250$ meV), 110 ± 10 meV, 140 ± 10 meV, 180 ± 10 meV, and 200 ± 10 meV ($E_i = 450$ meV). The scattering intensity is obtained after subtracting a radial background and has two-fold [(c),(g)] or fourfold symmetry [(h),(i)]. (d-f), (j-l) Corresponding constant-energy slices of dynamic magnetic structure factor $S(\mathbf{Q}, E)$ obtained from DFT+DMFT calculation. All data are taken at $T = 5$ K.

mined Fermi surfaces, where the low-energy spin excitations for Co-doped LiFeAs involve mostly the d_{xy} - d_{xy} character (Fig. S3) [31]. Similarly, spin excitations from the d_{yz} - d_{yz} channel are considerably reduced with the suppression of superconductivity.

Figure 3 summarizes the two-dimensional images of spin excitations at different energies and their comparison with DFT+DMFT calculations for LiFe_{0.88}Co_{0.12}As. Below $E = 25$ meV, spin excitations occur at $\mathbf{Q}_{AF} = (1, 0)$ and $(0, 1)$ positions similar to spin waves in NaFeAs [Fig. 3(a)] [28]. On increasing energy to $E = 67.5 \pm 7.5$ meV, spin excitations begin to split vertically from $(1, 0)$, again similar to spin waves of NaFeAs [Fig. 3(b)]. However, at energies above $E = 100$ meV, spin excitations in LiFe_{0.88}Co_{0.12}As form rings of scattering centered around $(\pm 1, \pm 1)$ which shrink slowly with increasing energy and persist up to $E = 200$ meV [Figs. 3(c), 3(g), 3(h), and 3(i)]. This is significantly different from NaFeAs, where spin waves reach the band top near 100 meV [28]. Since high-energy spin excitations in LiFeAs behave similarly [35], we conclude that spin excitations of LiFe_{1-x}Co_xAs have larger band width than that of NaFeAs [28], are

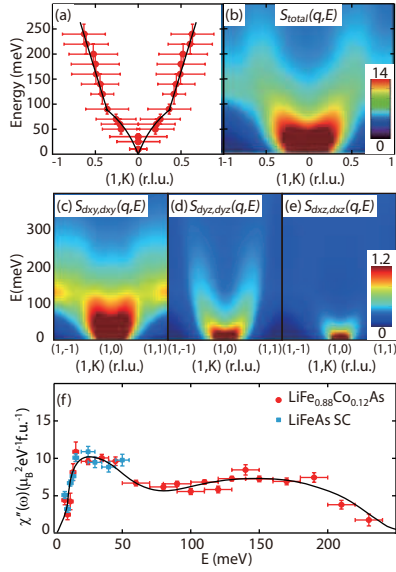


FIG. 4: (Color online) (a) The dispersion of spin excitations from time-of-flight neutron scattering data as seen in Fig. S2. The points represent the peak positions fitted with Gaussians. The errors in energy are the energy integration range and the \mathbf{Q} -errors come from the fitted peak width. (b) The corresponding total dynamic spin susceptibility calculated by DFT+DMFT. (c-e) The diagonal components of the dynamic magnetic structure factor $S_{xy,xy}(\mathbf{q}, E)$, $S_{yz,yz}(\mathbf{q}, E)$, and $S_{xz,xz}(\mathbf{q}, E)$ which originate from the d_{xy} , d_{yz} and d_{xz} orbitals, respectively. (f) Energy dependence of the measured local dynamic spin susceptibility for $\text{LiFe}_{0.88}\text{Co}_{0.12}\text{As}$ and superconducting LiFeAs at $T = 5$ K.

similar to that of $\text{BaFe}_{2-x}\text{Ni}_x\text{As}_2$ [37, 38]. Given the similar crystal structure and superconducting transition temperatures of $\text{LiFe}_{1-x}\text{Co}_x\text{As}$ [24] and $\text{NaFe}_{1-x}\text{Co}_x\text{As}$ [36], one would expect similar electron correlations and spin excitations band width in these two families of materials [39, 40].

To determine the spin excitation dispersions of $\text{LiFe}_{0.88}\text{Co}_{0.12}\text{As}$, we made a series of cuts on images of spin excitations in Fig. 3 along the $[1, K]$ direction at different energies (Fig. S2) [31] and extracted the dispersion as shown in Fig. 4(a). Compared with dispersions of spin waves in NaFeAs [28] and spin excitations in $\text{BaFe}_{2-x}\text{Ni}_x\text{As}_2$ [37, 38], dispersion of $\text{LiFe}_{0.88}\text{Co}_{0.12}\text{As}$ has distinctive features around 100 meV [Fig. 4(a)]. Figure 4(b) shows the DFT+DMFT calculated total dynamic spin dynamic susceptibility, which reveals clear two component structure similar to spin excitations in Fig. 4(a). Figures 4(c), 4(d), and 4(e) are dynamic spin susceptibility corresponding to the d_{xy} - d_{xy} , d_{xz} - d_{xz} , and d_{yz} - d_{yz} intra-orbital scattering channels between the hole and electron Fermi surfaces, respectively. Along the $(1, K)$ direction, spin excitations from the d_{xy} orbital reach zone boundary around $E = 130$ meV [Fig. 4(c)], while excitations from the d_{yz} orbital extend to energies well above $E = 200$ meV [along the $(K, 1)$ direction,

it would be the d_{xz} orbital component due to the four fold symmetry]. The similarities in Figures 4(a) and 4(b) strongly suggest that the upper and lower branches of the observed spin excitations have different orbital origins. In Figure 4(f), we compare the estimated local dynamic spin susceptibility for $\text{LiFe}_{0.88}\text{Co}_{0.12}\text{As}$ and LiFeAs at $T = 5$ K. The total fluctuating moment of $\text{LiFe}_{0.88}\text{Co}_{0.12}\text{As}$ is $\langle \mathbf{m}^2 \rangle = 1.5 \pm 0.3 \mu_B^2/\text{Fe}$. This is similar to superconducting LiFeAs [21–23], but is somewhat smaller than those of NaFeAs ($\langle \mathbf{m}^2 \rangle \approx 3.2 \mu_B^2/\text{Fe}$) [28] and BaFe_2As_2 ($\langle \mathbf{m}^2 \rangle \approx 3.6 \mu_B^2/\text{Fe}$) [41, 42]. This means that the total fluctuating moments for LiFeAs family of materials are smaller than those of NaFeAs and BaFe_2As_2 iron pnictides.

In iron pnictide such as BaFe_2As_2 , spin wave dispersions can be well described by an anisotropic Heisenberg Hamiltonian [41]. However, the two branch feature of the spin excitation dispersion in $\text{LiFe}_{0.88}\text{Co}_{0.12}\text{As}$ clearly cannot be satisfactorily fitted by this anisotropic Heisenberg model. Our neutron scattering experiments and DFT+DMFT calculations suggest that orbital selective quasiparticle excitations may account for the energy and wave vector dependence of spin excitations in $\text{LiFe}_{0.88}\text{Co}_{0.12}\text{As}$. This indicates that the superexchange spin interactions are different for different orbitals.

It is well known that electronic correlations in iron pnictides depend sensitively on the Fe pnictogen distance owing to the kinetic frustration mechanism of the Fe $3d$ electrons, and are strongly enhanced with increasing Fe-pnictogen distance [39, 40, 43]. Together with the large Hund's rule coupling and strong on-site Coulomb repulsion, the kinetic frustration mechanism also gives rise to the strong orbital differentiation of the electronic correlation strength [15, 39]. Orbital selective electronic correlation has been found in $\text{FeTe}_{1-x}\text{Se}_x$, where the effective mass of bands dominated by the d_{xy} orbital character decreases with increasing selenium as compared to the d_{xz}/d_{yz} bands [44]. In the case of LiFeAs , charge transfer from the d_{xy} to d_{xz}/d_{yz} orbitals can account for the Fermi surface topology of LiFeAs as the consequence of orbital dependent band renormalization [39, 45]. As shown in Fig. S6 [31], the increased pnictogen height in LiFeAs compared with NaFeAs narrows the electronic bandwidth of the d_{xy} orbital, which in turn transfers electrons from the d_{xy} to the d_{xz}/d_{yz} bands. The observed Co-doping dependence of low-energy spin excitations results from the d_{xy} - d_{xy} orbital dependent Fermi surface nesting. The narrow electronic bandwidth of the d_{xy} also leads to narrow bandwidth of spin excitations, and weak effective magnetic exchange coupling.

Since the d_{xy} orbital dominated Fermi surface nesting becomes better for $\text{LiFe}_{0.88}\text{Co}_{0.12}\text{As}$, low-energy spin excitations become commensurate with enhanced spectral weight compared to incommensurate spin excitations in LiFeAs [Fig. 1(b) and 1(d)]. This is consistent with NMR measurements [25] and RPA/DFT+DMFT calculations

(Figs. S3 and S4) [31]. The observed non-Fermi liquid behavior near $x = 0.12$ is then due to vanishing Fermi surface pocket associated with d_{yz}/d_{xz} orbitals as the Lifshitz transition is approached from the underdoped side [46]. In principle, an increased spin-fluctuation spectral weight should provide a larger electron pairing strength, and thus higher T_c within the spin-fluctuation mediated superconductivity scenario [4]. However, since Co-doping to LiFeAs also induces large incoherent electron scattering [26] and narrows the magnetic bandwidth in the d_{xy} orbital [Fig. 4(c)], superconductivity associated with the d_{xy} orbital may be prohibited due to reduced effective magnetic exchange coupling associated with the d_{xy} orbitals [29]. Similarly, in spite of the large magnetic bandwidth associated with the d_{xz}/d_{yz} orbitals, the poor Fermi surface nesting of these orbitals suppresses low energy spin excitations, which is also bad for superconductivity [29]. Therefore, superconductivity in iron pnictides can only occur with appropriate orbital selective low-energy spin excitations coupled with reasonable large magnetic exchange coupling.

The neutron scattering work at Rice is supported by the U.S. DOE, BES de-sc0012311 (P.D.). The computational work at Rice, ORNL, and Rutgers is supported by NSF DMR-1436006 (P.D.), DMR-1308603 (T.M.), DMR-1405303 (K.H.), and DMR-1308141 (Z.P.Y. and G.K.). The materials effort at Rice is also supported by the Robert A. Welch Foundation Grant Nos. C-1839 (P.D.). The research at SNS was sponsored by the Scientific User Facilities Division, BES, U.S. DOE. The research used resources of the Oak Ridge Leadership Computing Facility at ORNL, which is supported by U.S. DOE under Contract No. DE-AC05-00OR22725. The work at IOP, CAS is supported by NSFC and MOST of China through research projects.

* Electronic address: yinzhiping@bnu.edu.cn

† Electronic address: pdai@rice.edu

- [1] Y. Kamihara, T. Watanabe, M. Hirano, and H. Hosono, *J. Am. Chem. Soc.* **130**, 3296 (2008).
- [2] C. de la Cruz, Q. Huang, J. W. Lynn, J. Li, W. Ratcliff II, J. L. Zarestky, H. A. Mook, G. F. Chen, J. L. Luo, N. L. Wang, and P. C. Dai, *Nature* **453**, 899 (2008).
- [3] Q. Huang, Y. Qiu, Wei Bao, M. A. Green, J. W. Lynn, Y. C. Gasparovic, T. Wu, G. Wu, and X. H. Chen, *Phys. Rev. Lett.* **101**, 257003 (2008).
- [4] D. J. Scalapino, *Rev. Mod. Phys.* **84**, 1383 (2012).
- [5] P. C. Dai, *Rev. Mod. Phys.* **87**, 855 (2015).
- [6] X. Wang, Q. Liu, Y. Lv, W. Gao, L. Yang, R. Yu, F. Li, and C. Jin, *Solid State Commun.* **148**, 538 (2008).
- [7] M. J. Pitcher, D. R. Parker, P. Adamson, S. J. C. Herkelrath, A. T. Boothroyd, R. M. Ibberson, M. Brunelli, and S. J. Clarke, *Chem. Commun. (Cambridge)* **45**, 5918 (2008).
- [8] J. H. Tapp, Z. J. Tang, B. Lv, K. Sasmal, B. Lorenz, P. C.W. Chu, and A. M. Guloy, *Phys. Rev. B* **78**, 060505(R) (2008).
- [9] P. J. Hirschfeld, M. M. Korshunov, I. I. Mazin, *Rep. Prog. Phys.* **74**, 124508 (2011).
- [10] A. V. Chubukov, *Annu. Rev. Condens. Matter Phys.* **3**, 57 (2012).
- [11] Y. Wang, A. Kreisel, V. B. Zabolotnyy, S. V. Borisenko, B. Bchner, T. A. Maier, P. J. Hirschfeld, and D. J. Scalapino, *Phys. Rev. B* **88**, 174516 (2013).
- [12] T. Saito, S. Onari, Y. Yamakawa, H. Kontani, S. V. Borisenko, and V. B. Zabolotnyy, *Phys. Rev. B* **90**, 035104 (2014).
- [13] T. Saito, Y. Yamakawa, S. Onari, H. Kontani, *Phys. Rev. B* **92**, 134522 (2015).
- [14] K. Haule and G. Kotliar, *New J. Phys.* **11**, 025021 (2009).
- [15] A. Georges, L. De Medici, and J. Mravlje, *Annual Reviews of Condensed Matter Physics* **4**, 137 (2013).
- [16] C. C. Lee, W. G. Yin, and W. Ku, *Phys. Rev. Lett.* **103**, 267001 (2009).
- [17] F. Krüger, S. Kumar, J. Zaanen, and J. van den Brink, *Phys. Rev. B* **79**, 054504 (2009).
- [18] W. C. Lv, J. S. Wu, and P. Phillips, *Phys. Rev. B* **80**, 224506 (2009).
- [19] C.-C. Chen, J. Maciejko, A. P. Sorini, B. Moritz, R. R. P. Singh, and T. P. Devereaux, *Phys. Rev. B* **82**, 100504(R) (2010).
- [20] B. Valenzuela, E. Bascones, and M. J. Calderón, *Phys. Rev. Lett.* **105**, 207202 (2010).
- [21] N. Qureshi, P. Steffens, Y. Drees, A. C. Komarek, D. Lamago, Y. Sidis, L. Harnagea, H.-J. Grafe, S. Wurmehl, B. Buchner, and M. Braden, *Phys. Rev. Lett.* **108**, 117001 (2012).
- [22] M. Wang, M. Y. Wang, H. Miao, S. V. Carr, D. L. Abernathy, M. B. Stone, X. C. Wang, L. Y. Xing, C. Q. Jin, X. T. Zhang, J. P. Hu, T. Xiang, H. Ding, and P. C. Dai, *Phys. Rev. B* **86**, 144511 (2012).
- [23] N. Qureshi, P. Steffens, D. Lamago, Y. Sidis, O. Sobolev, R. A. Ewings, L. Harnagea, S. Wurmehl, B. Buchner, and M. Braden, *Phys. Rev. B* **90**, 144503 (2014).
- [24] M. J. Pitcher, T. Lancaster, J. D. Wright, I. Franke, A. J. Steele, P. J. Baker, F. L. Pratt, W. T. Thomas, D. R. Parker, S. J. Blundell et al., *J. Am. Chem. Soc.* **132**, 10467 (2010).
- [25] Y. M. Dai, H. Miao, L. Y. Xing, X. C. Wang, P. S. Wang, H. Xiao, T. Qian, P. Richard, X. G. Qiu, W. Yu, C. Q. Jin, Z. Wang, P. D. Johnson, C. C. Homes, and H. Ding, *Phys. Rev. X* **5**, 031035 (2015).
- [26] Z. R. Ye, Y. Zhang, F. Chen, M. Xu, J. Jiang, X. H. Niu, C. H. P. Wen, L. Y. Xing, X. C. Wang, C. Q. Jin, B. P. Xie, and D. L. Feng, *Phys. Rev. X* **4**, 031041 (2014).
- [27] H. Miao, T. Qian, X. Shi, P. Richard, T. K. Kim, M. Hoesch, L. Y. Xing, X.-C. Wang, C.-Q. Jin, J.-P. Hu, and H. Ding, *Nat. Comm.* **6**, 6056 (2015).
- [28] C. L. Zhang, L. W. Harriger, Z. P. Yin, W. C. Lv, M. Y. Wang, G. T. Tan, Y. Song, D. L. Abernathy, W. Tian, T. Egami, K. Haule, G. Kotliar, and P. C. Dai, *Phys. Rev. Lett.* **112**, 217202 (2014).
- [29] M. Wang, C. L. Zhang, X. Y. Lu, G. T. Tan, H. Q. Luo, Y. Song, M. Y. Wang, X. T. Zhang, E. A. Goremychkin, T. G. Perring, T. A. Maier, Z. P. Yin, K. Haule, G. Kotliar, and P. C. Dai, *Nat. Comm.* **4**, 2874 (2013).
- [30] S. L. Li, C. de la Cruz, Q. Huang, G. F. Chen, T.-L. Xia, J. L. Luo, N. L. Wang, and P. C. Dai, *Phys. Rev. B* **80**, 020504(R) (2009).

- [31] See Supplemental Material [url], which includes Refs. [47–56].
- [32] H. Q. Luo, Z. Yamani, Y. Chen, X. Y. Lu, M. Wang, S. L. Li, T. A. Maier, S. Danilkin, D. T. Adroja, and P. C. Dai, *Phys. Rev. B* **86**, 024508 (2012).
- [33] M. Yi, D. H. Lu, J.-H. Chu, J. G. Analytis, A. P. Sorini, A. F. Kemper, B. Moritz, S.-K. Mo, R. G. Moore, M. Hashimoto, W.-S. Lee, Z. Hussain, T. P. Devereaux, I. R. Fisher, and Z.-X. Shen, *PNAS* **108**, 6878 (2011).
- [34] S. V. Borisenko, V. B. Zabolotnyy, D. V. Evtushinsky, T. K. Kim, I. V. Morozov, A. N. Yaresko, A. A. Kordyuk, G. Behr, A. Vasiliev, R. Follath, and B. Buchner, *Phys. Rev. Lett.* **105**, 067002 (2010).
- [35] Meng Wang, X. C. Wang, D. L. Abernathy, L. W. Harriger, H. Q. Luo, Yang Zhao, J. W. Lynn, Q. Q. Liu, C. Q. Jin, C. Fang, J. P. Hu, and P. C. Dai, *Phys. Rev. B* **83**, 220515(R) (2011).
- [36] D. R. Parker, M. J. P. Smith, T. Lancaster, A. J. Steele, I. Franke, P. J. Baker, F. L. Pratt, M. J. Pitcher, S. J. Blundell, and S. J. Clarke, *Phys. Rev. Lett.* **104**, 057007 (2010).
- [37] M. S. Liu, L. W. Harriger, H. Q. Luo, M. Wang, R. A. Ewings, T. Guidi, H. Park, K. Haule, G. Kotliar, S. M. Hayden, and P. C. Dai, *Nat. Phys.* **8**, 376 (2012).
- [38] H. Q. Luo, X. Y. Lu, R. Zhang, M. Wang, E. A. Goremychkin, D. T. Adroja, S. Danilkin, G. Deng, Z. Yamani, and P. C. Dai, *Phys. Rev. B* **88**, 144516 (2013).
- [39] Z. P. Yin, K. Haule, and G. Kotliar, *Nat. Mater.* **10**, 932 (2011).
- [40] Z. P. Yin, K. Haule, G. Kotliar, *Nat. Phys.* **10**, 845 (2014).
- [41] L. W. Harriger, H. Q. Luo, M. S. Liu, C. Frost, J. P. Hu, M. R. Norman, and P. C. Dai, *Phys. Rev. B* **84**, 054544 (2011).
- [42] L. W. Harriger, M. Liu, H. Luo, R. A. Ewings, C. D. Frost, T. G. Perring, and P. C. Dai, *Phys. Rev. B* **86**, 140403(R) (2012).
- [43] Y. K. Kim, Y. Y. Koh, W. S. Kyung, G. R. Han, B. Lee, Kee Hoon Kim, J. M. Ok, Jun Sung Kim, M. Arita, K. Shimada, H. Namatame, M. Taniguchi, S.-K. Mo, and C. Kim, *Phys. Rev. B* **92**, 041116(R) (2015).
- [44] Z. K. Liu, M. Yi, Y. Zhang, J. Hu, R. Yu, J.-X. Zhu, R.-H. He, Y. L. Chen, M. Hashimoto, R. G. Moore, S.-K. Mo, Z. Hussain, Q. Si, Z. Q. Mao, D. H. Lu, and Z.-X. Shen, *Phys. Rev. B* **92**, 235138 (2015).
- [45] Geunsik Lee, Hyo Seok Ji, Yeongkwan Kim, Changyoung Kim, Kristjan Haule, Gabriel Kotliar, Bumsung Lee, Seunghyun Khim, Kee Hoon Kim, Kwang S. Kim, Ki-Seok Kim, and Ji Hoon Shim, *Phys. Rev. Lett.* **109**, 177001 (2012).
- [46] S. D. Das, M. S. Laad, L. Craco, J. Gillett, V. Tripathi, and S. E. Sebastian, *Phys. Rev. B* **92**, 155112 (2015).
- [47] L. Y. Xing, H. Miao, X. C. Wang, J. Ma, Q. Q. Liu, Z. Deng, H. Ding, and C.Q. Jin, *J. Phys.: Condens. Matter* **26**, 435703 (2014).
- [48] D. R. Parker, M. J. Pitcher, P. J. Baker, I. Franke, T. Lancaster, S. J. Blundell, and S. J. Clarke, *Chem. Commun.*, 2189 (2009) (DOI: 10.1039/B818911K).
- [49] H. Eschrig and K. Koepf, *Phys. Rev. B* **80**, 104503 (2009).
- [50] K. Kuroki, S. Onari, R. Arita, H. Usui, Y. Tanaka, H. Kontani, and H. Aoki, *Phys. Rev. Lett.* **101**, 087004 (2008).
- [51] P. Blaha, K. Schwarz, G. K. H. Madsen, D. Kvasnicka and J. Luitz, WIEN2K (K. Schwarz, Techn. Univ. Wien, Austria, 2001).
- [52] J. P. Perdew, K. Burke, and M. Ernzerhof, *Phys. Rev. Lett.* **77**, 3865 (1996).
- [53] G. Kotliar, S. Y. Savrasov, K. Haule, V. S. Oudovenko, O. Parcollet, and C. A. Marianetti, *Rev. Mod. Phys.* **78**, 856 (2006).
- [54] K. Haule, C.-H. Yee, K. Kim, *Phys. Rev. B* **81**, 195107 (2010).
- [55] K. Haule, *Phys. Rev. B* **75**, 155113 (2007).
- [56] P. Werner, A. Comanac, L. de Medici, M. Troyer, and A. J. Millis, *Phys. Rev. Lett.* **97**, 076405 (2006).

Supplementary Information:

SAMPLE PREPARATION

$\text{LiFe}_{1-x}\text{Co}_x\text{As}$ single crystals were grown with self-flux method. The basic sample characterization was described in the previous papers [S1, S2]. Samples used in this report were grown with isotope ^7Li to reduce the neutron absorption and wrapped by Aluminum foil with Hydrogen-free glue to avoid exposure to air and humidity. The sample growth work was carried out at Beijing National Laboratory for Condensed Matter Physics, Institute of Physics, Chinese Academy of Science and at Rice University.

BACKGROUND SUBTRACTION AND DATA ANALYSIS

In a typical time-of-flight experiment, the raw inelastic neutron scattering data at certain energy are shown in Fig. S1(a). In order to obtain the background, we masked the signal area, for instance, the white square in Fig. S1(b). Assuming the background in our time-of-flight data is radially symmetric, we integrated the remaining intensity and fitted it with a polynomial function of $|Q|$ to the second order as shown in Fig. S1(c). Then we used this fitted polynomial function as background and subtracted it from the raw neutron scattering data. The final subtracted data was shown in Fig. S1(d) and Fig. S1(e).

In Fig. S2, we show a series of typical subtracted constant-energy cuts from 10 meV to 220 meV. These cuts were fitted with one or two Gaussian functions. We show the fitted result in previous Fig. 4(a). It is worth noting that the x-errors in Fig. 4(a) are the fitted peak width.

RPA CALCULATION

In Fig. S3, we demonstrate the existence of two transversely incommensurate peaks in the dynamic spin susceptibility with differentiated orbital character for LiFeAs . Electron-doping in $\text{LiFe}_{0.88}\text{Co}_{0.12}\text{As}$ is introduced by rigid band shift. The starting point for our calculation is an effective 10-orbital tight-binding Hamiltonian derived from ARPES and symmetry considerations [S4] and previously discussed in Ref. [S5]. We calculate the noninteracting bare susceptibility along high-symmetry cuts, considering lowest-order scattering processes as described previously [S5, S6]:

$$\chi_{l_1 l_2 l_3 l_4}^0(q, \omega) = -\frac{1}{N} \sum_{k, \mu \nu} \frac{a_{\mu}^{l_4}(k) a_{\mu}^{l_2,*}(k) a_{\nu}^{l_1}(k+q) a_{\nu}^{l_3,*}(k+q)}{\omega + E_{\mu}(k) - E_{\nu}(k+q) + i\delta} (f[E_{\mu}(k), kT] - f[E_{\nu}(k+q), kT]) \quad (\text{S1})$$

with $N = 2$ the number of iron sites per unit cell, band indices μ and ν , orbital indices l . The matrix elements are represented by the orbital projection of the Bloch state, $a_{\mu}^l = \langle l | \mu k \rangle$ and $f[E, kT]$ is the Fermi function at temperature T . We use $T = 100$ K, a small parameter $\delta = 0.005$ to enforce analyticity, and sum over a k -space mesh of $120 \times 120 \times 8$ points over the 3D Brillouin zone, which we find to be sufficiently dense to accurately describe the susceptibility everywhere in reciprocal space.

RPA interactions are applied in a manifestly spin-rotationally invariant form, using the intra-orbital Coulomb repulsion $U = 0.6$ eV and Hund's coupling $J = 0.15$, and inter-orbital Coulomb interaction $U' = 0.3$ and pair-hopping $J' = 0.15$, with the same interaction strengths applied identically over all ten d-orbitals. These values for the interactions are just below their maximum values, as determined when the susceptibility diverges at the antiferromagnetic wave vector Q in the doped compound. Because the intraorbital scattering is dominant in the total RPA susceptibility, we focus on intra-orbital components of the bare susceptibility in the low energy limit, $\chi^0(q, \omega = 10 \text{ meV})$. To enable direct comparison to neutron scattering, where the orthorhombic structure factor forbids scattering at even L , we fix $q_z = \frac{\pi}{c}$ ($L=1$).

We find the scattering peaks in the parent compound ($\langle n \rangle = 12.00$) at $\Delta Q \approx 0.18$ and 0.3 , quite consistent with the incommensurabilities suggested by Fermi surface nesting shown in Fig. 1(c)-(d). After the application of RPA interactions, tracing only over the d_{xy} (d_{xz}) orbitals selectively amplifies the narrower (wider) peaks; in other words, considering the system with and without interactions, the results are qualitatively identical. In the electron-doped case ($\langle n \rangle = 12.24$), the single obvious feature is the commensurate peak, which has predominantly d_{xy} character.

DFT+DMFT CALCULATION

Density functional theory (DFT) calculations were done using the full-potential linear augmented plane wave method implemented in Wien2K[S7] in conjunction with a generalized gradient approximation[S8] of the exchange correlation functional. To take into account strong correlation effect, we further carried out first principles calculations using a combination of density functional theory and dynamical mean field theory (DFT+DMFT)[S9] which was implemented on top of Wien2K and documented in Ref. [S10]. In the DFT+DMFT calculations, the electronic charge was computed self-consistently on DFT+DMFT density matrix. The quantum impurity problem was solved by the continuous time quantum Monte Carlo (CTQMC) method[S11, S12], using Slater form of the Coulomb repulsion in its fully rotational invariant form. Consistent with previous publication[S13, S14], we used a Hubbard $U=5.0$ eV and Hund's rule coupling $J=0.8$ eV, and experimentally determined crystal structure for LiFeAs[S15], including the internal positions of the atoms. The Co-doping is simulated using virtual crystal approximation (VCA) in the DFT+DMFT calculation. The bare susceptibility was computed using the fully self-consistent DFT+DMFT lattice Green's function and the spin susceptibility was computed using the Bethe-Salpeter equation which takes into account two particle vertex correction. Here the two-particle (particle-hole) irreducible vertex is local within DMFT and it is equal to the impurity vertex, which can be obtained from the solution of the quantum impurity model using CTQMC. Further computational details on spin susceptibility are available in Ref.[S14].

* Electronic address: yinzhiping@bnu.edu.cn

† Electronic address: pdai@rice.edu

- [S1] L.Y. Xing, H Miao, X.C. Wang, J Ma, Q.Q. Liu, Z. Deng, H. Ding and C.Q. Jin, J.Phys.: Condens. Matter **26**, 435703 (2014)
- [S2] Michael J. Pitcher, Dinah R. Parker, Paul Adamson, Sebastian J.C. Herkelrath, Andrew T. Boothroyd, Richard M. Ibberson, Michela Brunelli and Simon J. Clarke, Chem. Commun., **2008**, 5918C5920
- [S3] D. R. Parker, M. J. Pitcher, P. J. Baker, I. Franke, T. Lancaster, S. J. Blundell, and S. J. Clarke, Chem. Commun., **2009**, 2189C2191
- [S4] H. Eschrig and K. Koepernik, Phys. Rev. B **80**, 104503 (2009).
- [S5] Y. Wang, A. Kreisel, V. Zabolotnyy, S. Borisenko, B. Bchner, T. Maier, P. Hirschfeld, and D. Scalapino, Phys. Rev. B **88**, 174516 (2013)
- [S6] K. Kuroki, S. Onari, R. Arita, H. Usui, Y. Tanaka, H. Kontani, and H. Aoki, Phys. Rev. Lett. **101**, 087004 (2008)
- [S7] P. Blaha, K. Schwarz, G. K. H. Madsen, D. Kvasnicka and J. Luitz, **WIEN2K** (K. Schwarz, Techn. Univ. Wien, Austria, 2001)
- [S8] J. P. Perdew, K. Burke, and M. Ernzerhof, Phys. Rev. Lett. **77**, 3865-3868 (1996)
- [S9] G. Kotliar, S. Y. Savrasov, K. Haule, V. S. Oudovenko, O. Parcollet, and C. A. Marianetti, Rev. Mod. Phys. **78**, 856 (2006).
- [S10] K. Haule, C.-H. Yee, K. Kim, Phys. Rev. B **81**, 195107 (2010)
- [S11] Kristjan Haule, Phys. Rev. B **75**, 155113 (2007)
- [S12] P. Werner, A. Comanac, L. de Medici, M. Troyer, and A. J. Millis, Phys. Rev. Lett. **97**, 076405 (2006).
- [S13] Z. P. Yin, K. Haule, and G. Kotliar, Nat. Mater. **10**, 932 (2011)
- [S14] Z. P. Yin, K. Haule, G. Kotliar, Nat. Phys. **10**, 845 (2014).
- [S15] J. H. Tapp, Zhongjia Tang, Bing Lv, Kalyan Sasmal, Bernd Lorenz, Paul C.W. Chu, and Arnold M. Guloy, Phys. Rev. B **78**, 060505(R) (2008)

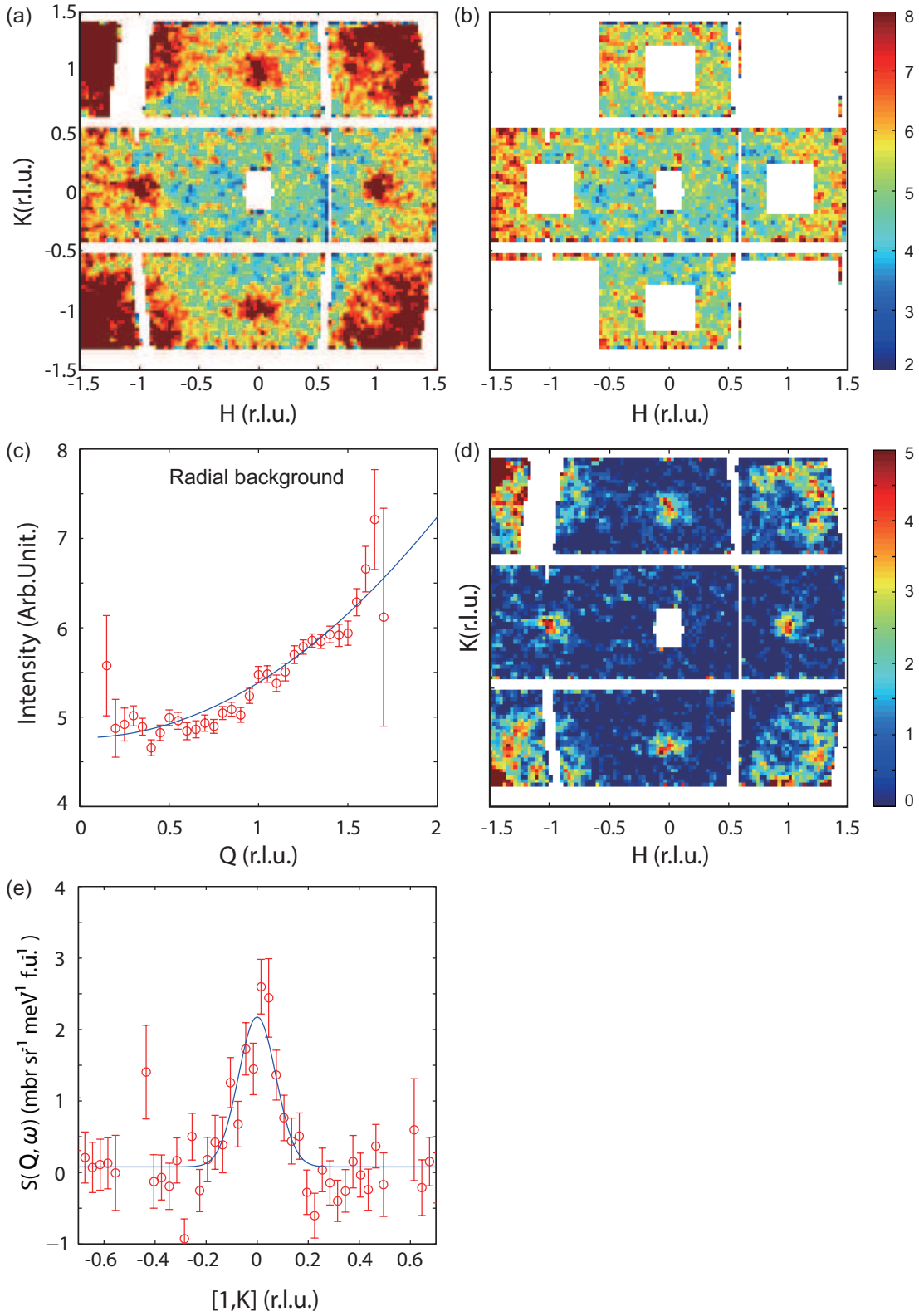


FIG. 1: (Color online) (a).Constant energy map of the raw data at $E=[6,8]$ meV in $\text{LiFe}_{0.88}\text{Co}_{0.12}\text{As}$. (b) The background intensity in which all the phonon and magnon signals are masked. (c) We get the radially symmetric background from (b) and fit it with a parabolic function. (d) The constant energy map after background subtraction. (e) A cut along $[1,H]$ direction in panel (d).

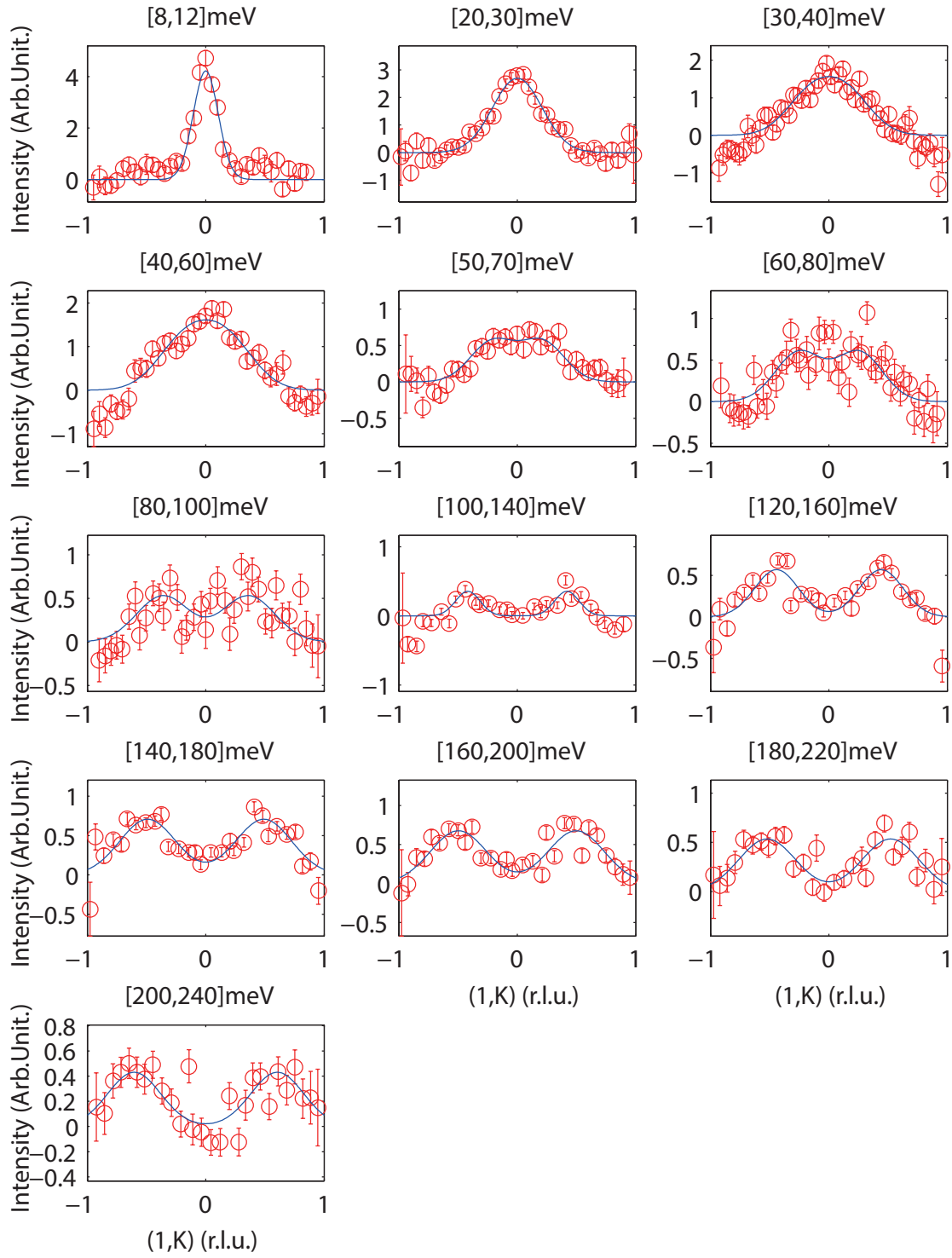


FIG. 2: (Color online) Energy dependence of the 1-d cut of the spin excitations along $[1, K]$ direction in $\text{LiFe}_{0.88}\text{Co}_{0.12}\text{As}$. The peaks are fitted with Gaussian functions and the fitted results are shown in Fig. 4(a). The energy ranges shown here are the E-errors and the peak widths are q-errors Fig. 4(a).

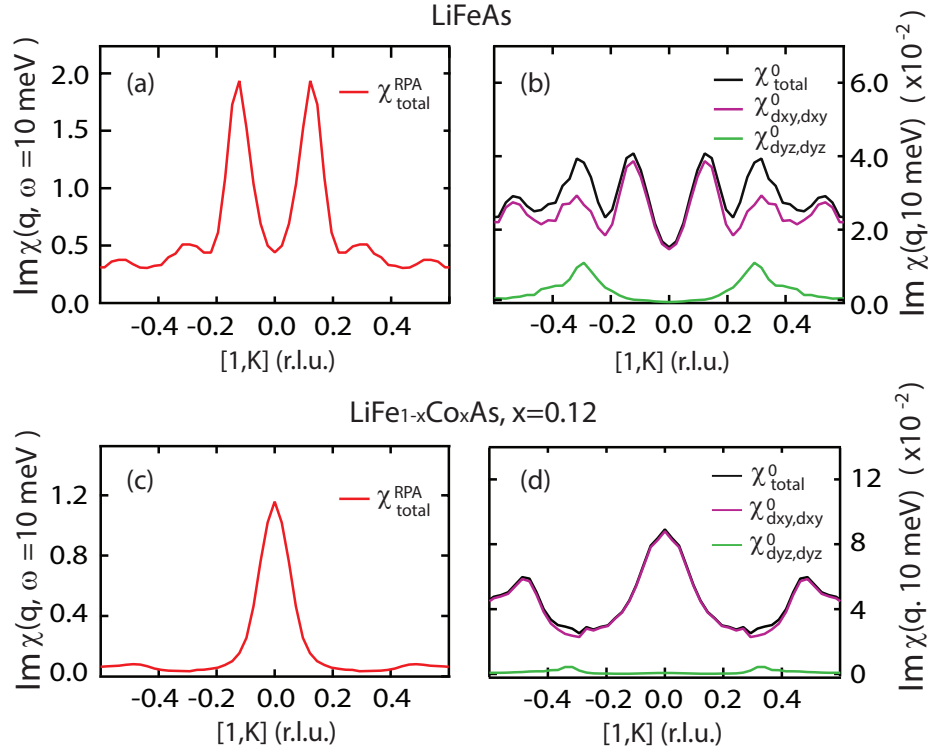


FIG. 3: (Color online) LDA+RPA calculation of dynamic spin susceptibility in LiFeAs and LiFe_{0.88}Co_{0.12}As. (a),(c) Wave vector dependence of the imaginary part of total RPA susceptibility at 10 meV for LiFeAs and LiFe_{0.88}Co_{0.12}As. Note that the peak position changes from incommensurate wave vector in LiFeAs to commensurate in 12% electron doped compound, consistent with our experimental result (Fig.1 (b)). (b),(d) The calculated bare susceptibility of LiFeAs and LiFe_{0.88}Co_{0.12}As. The black curve represents the total bare susceptibility while the purple (green) one shows the intra-orbital component of d_{xy} (d_{yz}) orbital. Note that the main peaks observed in LiFeAs mainly come from $\chi_{xy,xy}$ scattering channel while the $\chi_{yz,yz}$, (or $\chi_{xz,xz}$ due to the existence of four-fold symmetry) component almost vanishes when T_c is suppressed in LiFe_{0.88}Co_{0.12}As.

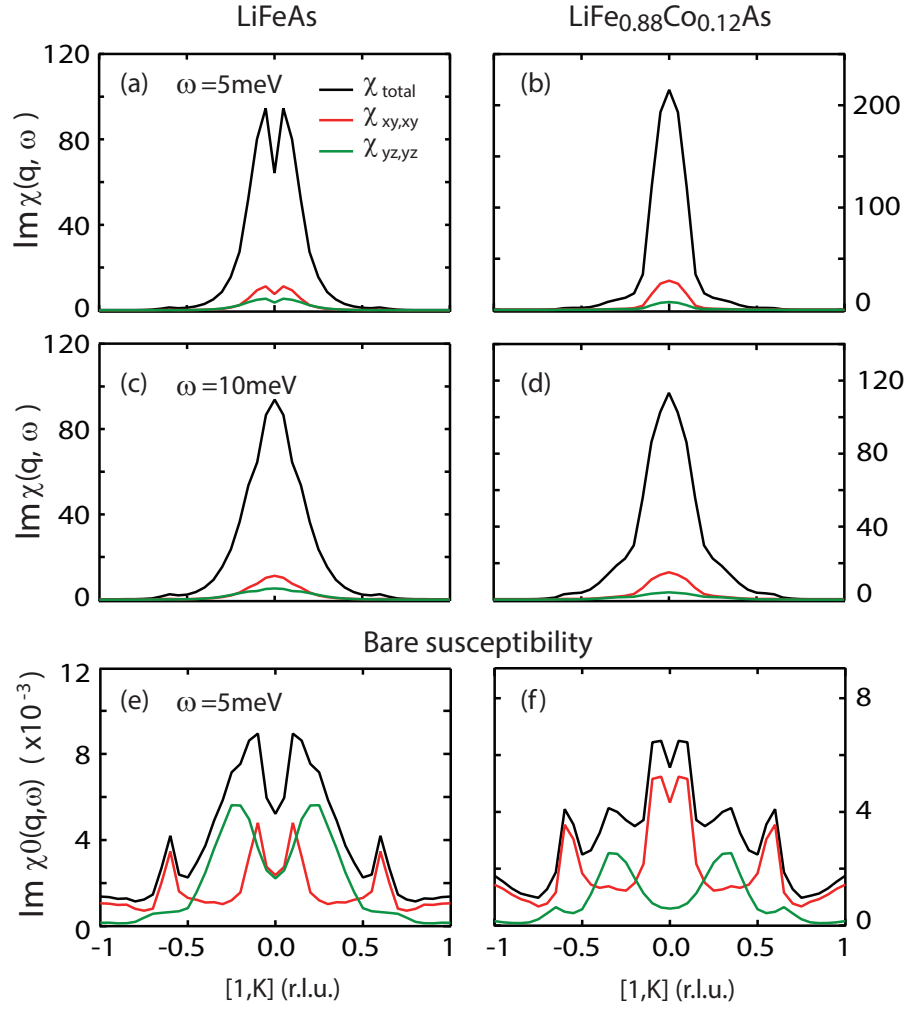


FIG. 4: (Color online) The dynamic spin susceptibility from DFT+DMFT calculation for LiFeAs and LiFe_{0.88}Co_{0.12}As. (a),(b) The imaginary part of spin susceptibility at 5 meV for LiFeAs and LiFe_{0.88}Co_{0.12}As, respectively. The black curves represent the total susceptibility and the red (green) ones are the $\chi_{xy,xy}$ ($\chi_{yz,yz}$) components. (c),(d) The corresponding total and orbital components of spin susceptibility at 10 meV for LiFeAs and LiFe_{0.88}Co_{0.12}As, respectively. (e), (f) are bare susceptibility for LiFeAs and LiFe_{0.88}Co_{0.12}As, respectively, at 5 meV. The doping dependence of the incommensurability is similar to the experimental result and LDA+RPA calculation. Note that in 12% Co doped compound, the $\chi_{xy,xy}$ component is actually enhanced while $\chi_{yz,yz}$ component is suppressed. The overall intensity of total susceptibility within this energy range is also enhanced a little bit, in sharp contrast to great suppression the superconducting temperature (T_c) in this compound.

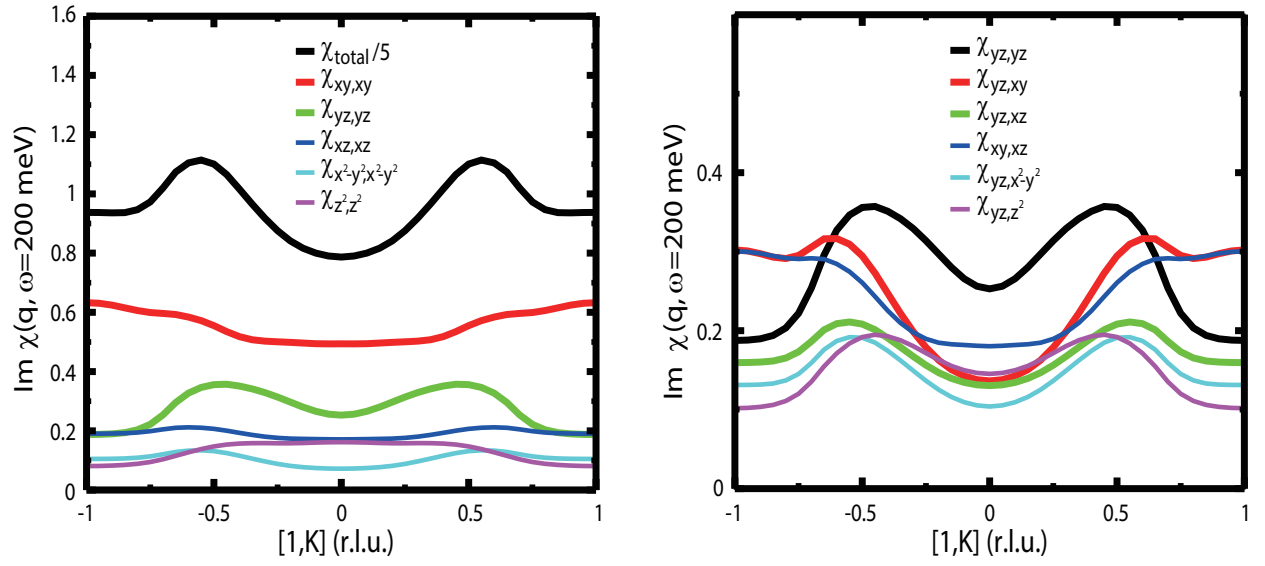


FIG. 5: (Color online) (a) The intra-orbital components of dynamic susceptibility at 200 meV (mainly upper branch) for $\text{LiFe}_{0.88}\text{Co}_{0.12}\text{As}$. It is clearly seen that the peaks in the total susceptibility mainly come from $\chi_{yz,yz}$ intra-orbital part. (b) Comparison between intra-orbital and inter-orbital components which are associated with d_{yz} orbital. The intra-orbital $\chi_{yz,yz}$ component is apparently dominant while the interorbital channels contribute a small part in the total spin susceptibility at 200 meV.

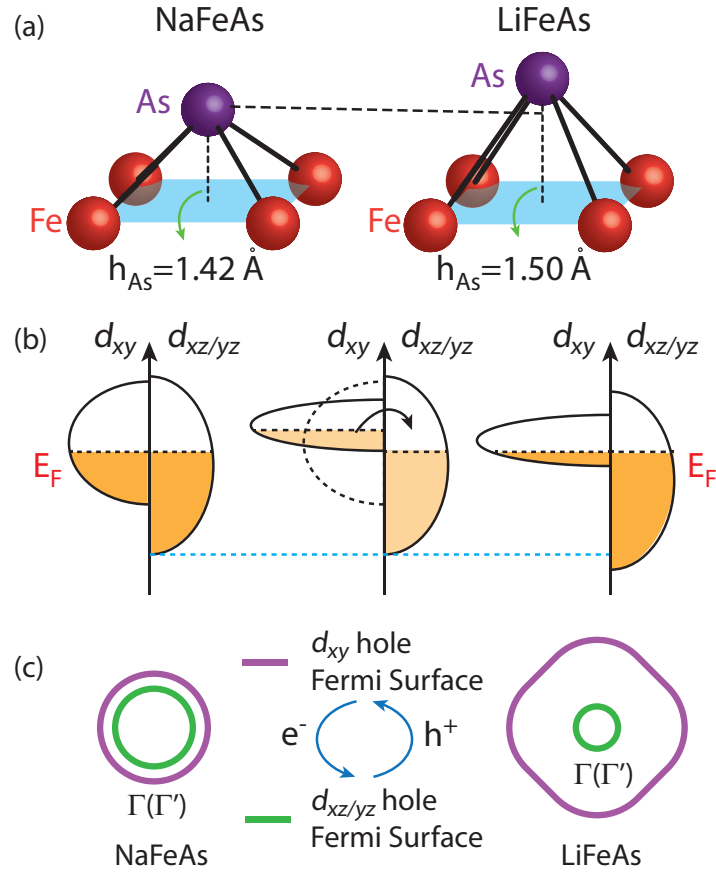


FIG. 6: (Color online) (a) The structure of the Fe-As layer in NaFeAs and LiFeAs. The anion height in LiFeAs $\sim 1.5 \text{ \AA}$ (Ref. [S2]) is larger than that in NaFeAs 1.42 \AA (Ref. [S4]). (b) Illustration of the orbital dependent band renormalization and subsequent charge transfer from d_{xy} to $d_{xz/yz}$ orbitals. The renormalization is overstated to emphasize the orbital dependent effect. The situation in reality might be even more complicated due to the strong hybridization with As p orbitals [S6]. (c) Comparison of the Fermi Surface in NaFeAs and LiFeAs. The orbital dependent band renormalization (panel (b)) drives electrons (holes) from d_{xy} ($d_{xz/yz}$) to $d_{xz/yz}$ (d_{xy}), resulting in an enlarged outer d_{xy} hole FS and a reduced inner $d_{xz/yz}$ pockets in LiFeAs.